Establishment of a longitudinally tractable mouse model of cholestatic liver injury via drinking water administration of MDA

Takumi Iwasaka[1], Katsuhisa Morita[1], Iori Azuma[1], Tomoka Nakagawa[1], Eri Nakashima[1], Tomomi Kamei[2], Yuki Kato[2], Hiroyuki Kusuhara[1], Tadahaya Mizuno[3, †]

[1]Graduate School of Pharmaceutical Sciences, the University of Tokyo, Bunkyo-ku, Tokyo, 113-0033, Japan
[2]Laboratory for Drug Discovery and Development, SHIONOGI & Co.,Ltd. Toyonaka, Osaka, 561-0825, Japan,
[3]Graduate School of Pharmaceutical Sciences, the University of Tokyo, Bunkyo-ku, Tokyo, 113-0033, Japan, Electronic address: tadahaya@gmail.com
†Corresponding author: Tadahaya Mizuno

Author Contributions
TI: Data curation, Formal analysis, Investigation, Writing – Original draft, Visualization.
KM: Investigation, Data curation
IA: Investigation, Data curation
TN: Investigation
EN: Investigation
TK: Formal analysis
YK: Formal analysis, Writing – Original draft, Writing – Review and editing
HK: Writing – Review and editing.
TM: Conceptualization, Resources, Supervision, Project administration, Writing – Original draft, Writing – Review and editing, Funding acquisition.

Address for Correspondence
tadahaya@gmail.com; Graduate School of Pharmaceutical Sciences, the University of Tokyo, Bunkyo-ku, Tokyo, 113-0033, Japan; Tel: +81-3-5841-4771

Financial support and sponsorship
This work was supported by the JSPS KAKENHI Grant-in-Aid for Scientific Research (C) (grant number 21K06663) and PAGS (grant number JP22H04925) from the Japan Society for the Promotion of Science, Takeda Science Foundation, and Mochida Memorial Foundation for Medical and Pharmaceutical Research.

Conflicts of interest
TK and YK are employees of Shionogi & Co., Ltd., which partially funded this study. All other authors declare no competing interests.

Keywords (< 5 words)
focal necrosis, multi-view data, immune cell profiling, RNA-seq, transcriptomic trajectory

List of Abbreviations
MDA, 4,4'-methylenedianiline; TAA, thioacetamide; ALT, alanine aminotransferase; AST, aspartate aminotransferase; GO, Gene Ontology; GAGE, Generally Applicable Gene-set Enrichment; ANIT, α-naphthylisothiocyanate; HSCs, hepatic stellate cells; PFs, portal fibroblasts

Abstract

Background & Aims:

Longitudinal animal models are essential for understanding the temporal dynamics of liver injury and recovery. While drinking water-based administration is ideal for sustained exposure in high feasibility, available compounds are limited, with thioacetamide (TAA) being the primary option. Here, we aimed to establish a novel drinking water-induced mouse model of cholestatic liver injury using 4,4'-methylenedianiline (MDA), and to characterize its pathological trajectory in comparison to the TAA model.

Methods:

Mice were administered MDA via drinking water for 28 Days. To elucidate the early events that give rise to chronic pathological divergence, we conducted a multi-layered analysis comprising plasma biochemical assays, immune cell profiling by flow cytometry, and hepatic transcriptomics at five time points during the early phase. The MDA model was evaluated against the established TAA model.

Results:

MDA administration led to sustained ALT elevation, peribiliary fibrosis, and spatially irregular focal hepatocellular necrosis, in contrast to the centrilobular injury observed with TAA. Early-phase analysis revealed increased serum ALP and TBIL, enhanced fibrinolysis-related gene signatures, and a lack of eosinophil accumulation in the MDA-administered mice. These early molecular and immunological differences are likely to underpin the model-specific chronic pathological outcomes.

Conclusions:

We present the MDA model as the first drinking water-based cholestatic liver injury model that is longitudinally tractable and mechanistically distinct from TAA. This model provides a versatile platform for studying the temporal dynamics of liver disease progression and resolution.

Introduction

Liver injury remains a major health concern due to its potential progression to cirrhosis, liver failure, and hepatocellular carcinoma, particularly when progression occurs over a prolonged, subclinical course. Understanding such longitudinal dynamics and cholangiopathies requires models capable of capturing both temporal evolution and diverse pathological phenotypes. These outcomes can arise from a wide range of etiologies, including viral infections, alcohol abuse, metabolic disorders, and, notably, drug-induced liver injury (DILI) (1,2). To better understand the mechanisms underlying liver pathology and to evaluate therapeutic strategies, animal models that replicate key aspects of human liver disease are indispensable. Among various approaches, chemical-induced models are widely utilized for their simplicity, reproducibility, and capacity to induce diverse pathological phenotypes (3).

Compounds such as carbon tetrachloride (CCl_4) and thioacetamide (TAA) have traditionally been used to induce liver injury and fibrosis, and these models have significantly advanced the field of experimental hepatology (4–10). However, many of these models rely on repeated injections or intraperitoneal administration, which not only increase the experimental personnel and burden on animals but also complicate long-term and time-resolved studies. Continuous compound administration via drinking water presents an attractive alternative that allows for stable exposure, cost-effective experimental design, and reduced procedural stress, particularly for longitudinal investigations.

Among drinking water-based models, the TAA drinking water (TAA-DW) model has been most widely adopted due to its ability to induce both acute and chronic liver injury (11,12). Nevertheless, reliance on a single compound limits both the diversity of pathological phenotypes and the ability to model cholestatic liver injury or trace pathophysiological transitions across time. For example, TAA predominantly induces centrilobular necrosis and offers limited tractability for studying biliary injury or longitudinal immune-molecular dynamics. Thus, expanding the repertoire of drinking water-administered hepatotoxins is a promising avenue to enhance the versatility of chemically induced liver injury models. However, whether alternative compounds can establish a stable, reproducible liver injury model through oral exposure remains largely unexplored.

To address this, we sought to identify and evaluate a new drinking water-based liver injury model using a compound distinct from TAA. Through data mining of toxicological databases and literature screening, we selected 4,4'-methylenedianiline (MDA) as a promising candidate. MDA has documented hepatotoxicity in oral dosing studies, yet has never been formally investigated as a drinking water-administered liver injury model (10,13). We administered MDA to mice via drinking water over 28 Days and evaluated the resulting liver injury in comparison to the established TAA-DW model.

The newly established MDA drinking water (MDA-DW) model consistently elevated ALT levels and revealed distinct histopathological features, including spatially irregular focal hepatocellular necrosis and peribiliary fibrosis, which differed markedly from the centrilobular-dominant injury seen in the TAA-DW model. We also investigated early-phase pathophysiological differences to better understand the basis of the chronic-phase divergence observed between models. To this end, we performed an integrated multi-

view analysis that combined systemic biochemical markers, immune cell profiling by flow cytometry, and hepatic transcriptomic profiling. This approach revealed distinct early responses that likely shape the subsequent progression and histological outcomes unique to each model.

Collectively, this study introduces the MDA-DW model as a novel, cholestatic liver injury model that is both easily implemented and longitudinally tractable. Its distinct pathological trajectory and compatibility with multi-layered, time-resolved analyses make it a valuable platform for exploring disease progression, resolution mechanisms, and therapeutic response in experimental hepatology.

Methods

Screening of candidate compounds for drinking water-induced liver injury model

Through database searches (CEBS, Open TG-GATEs, and DrugMatrix), compounds with ALT levels surpassing 200 U/L were extracted through administration regardless of route and time (14–16). Refined selection criteria with literature survey included: (a) the ability to induce liver dysfunction via oral administration, (b) water solubility (Solubility 1.0 g/L or greater), (c) cost-effectiveness, and ease of handling, and (d) a toxicity profile distinct from TAA, an existing drinking water-induced liver injury model.

Preparation of drug-induced liver injury models

Six-week-old male C57BL/6JJcl mice were purchased from CLEA Japan (Tokyo, Japan) and acclimatized for three to five Days. The mice were exposed to Thioacetamide (T0817, Tokyo Chemical Industry Co., Japan) or Methylene dianiline (M0220, Tokyo Chemical Industry Co., Japan) dissolved in drinking water (300 mg/l or 750 mg/l) to induce liver damage, whereas the controls received a tap water. The water intake of each treatment group is shown in Fig. S1. Mice were sacrificed at each time point and perfused liver samples and blood were harvested (Liver and blood sample collection section). The procedures reported in this article were performed in accordance with the guidelines provided by the Institutional Animal Care Committee (Graduate School of Pharmaceutical Sciences, the University of Tokyo, Tokyo, Japan).

Liver and blood sample collection

Through this study, the starting Day of administration is designated as Day 0. In the early phase (Days 1, 2, 3, 4, and 8), the blood was collected under isoflurane anesthesia through an inferior vena cava into 1.5 mL tube containing 1 μL heparin (Yoshindo Inc, Toyama, Japan) and a superior vena cava was clipped using a clamp. After cutting the portal vein, the first perfusion was performed by injecting 10 mL of 5 mM HEPES (H4034, Sigma-Aldrich Co. LLCUSA) / 5 mM EDTA (345-01865, Fujifilm Corporation) Hanks' Balanced Salt Solution (17461-05, Nacalai Tesque, INC., Japan) through the inferior vena cava. Then, the second perfusion was performed by using 10 mL of 5 mM HEPES Hanks' Balanced Salt Solution. Before harvesting the tissue, 2 mL of dissociation enzyme solution of gentleMACS (Miltenyi Biotec, Germany) was filled in the liver from an inferior vena cava with clipping the cut portal vein. In the chronic phase (Days 7, 14 and 28), the same process is performed up to the point before perfusion, the perfusion was performed by injecting 20 mL of phosphate-buffered saline (PBS) through the inferior vena cava. For the obtained liver, a portion of the outer left latera lobe of the liver was subjected to RNA isolation (RNA-seq or qPCR analysis section) and the remaining tissue to flow cytometry analysis (Flow cytometry analysis section, acute phase only) or to histopathological analysis (Histopathology section), respectively. When observing the temporal changes in the blood biochemical values of the same individual, blood samples were collected from the tail vein. Details about data analysis are available in Supplementary Information.

Analysis of blood specimens

The collected blood sample was centrifuged (1,700 g, 4 °C for 15 min) for serum separation. Serum level of alanine aminotransferase (ALT), aspartate aminotransferase (AST), alkaline phosphatase (ALP), total bilirubin (TBIL), total cholesterol (TCHO), and triglycerides (TG) were measured using a DRI-CHEM NX500sV (Fujifilm Corporation, Japan). If the upper limit is exceeded, dilute with 100 mM HEPES with 0.1% CHAPS (pH 7.4, r.t.) and re-measured.

Analysis of liver specimens

Detailed procedures of RNA-seq analysis, Histopathology and flow cytometry analysis, including subsequent data analysis, are provided in Supplementary Information.

Quantitative PCR analysis

Total RNA was prepared using ISOGEN II (311-07361, Nippon Gene Co., Ltd., Tokyo, Japan). RNA was reverse transcribed into cDNA using ReverTra Ace (TOYOBO, FSQ-301). Real-time PCR was performed using the THUNDERBIRD® Next SYBR® qPCR Mix (TOYOBO, QPX-201). Target gene expression was normalized to housekeeping genes Gapdh. Primers are listed in Table S1.

Clustering Analysis

Dimensionality reduction was performed using transcriptomic and flow cytometry data from the liver at Days 1, 2, 3, 4, and 8 after administration as input features. All features were reduced in dimensionality by principal component analysis, multidimensional scaling, t distributed stochastic neighbor embedding, uniform manifold approximation and projection, spectral embedding and locally linear embedding. The dimensionally reduced features were combined using a meta-visualization method (17). The combined meta-distance matrix was visualized with a scatter plot, with each point color-coded by time and dose condition or ALT value. Note that transcriptome features were log-transformed. The detailed code used is found on GitHub (https://github.com/mizuno-group/MDAdrinkingwater). Analysis was performed using Python (version 3.10.6) with open-source packages (numpy, version 1.24.4; pandas, version 2.0.3; scipy, version 1.11.1; scikit-learn, version 1.1.2; statsmodels, version 0.13.2; umap, version 0.5.4)

Gene Set Analysis

First, the Gene Ontology (GO) annotation file (m5.go.v2023.1.Mm.symbols.gmt) was downloaded from the MSigDB website (https://www.gsea-msigdb.org/gsea/msigdb) and used for the following analysis (18). In this part, the genes included in this GO annotation file were the genes to be analyzed. The transcriptome data were log-transformed, and genes with less than 70% (50 individuals) confirmed to be expressed were deleted. Subsequently, if the individuals with zero expression was biased toward a particular group by analysis of variance (one-way repeated measures ANOVA), that genes was retained.

Finally, missing values were complemented using KNNImputer (sklearn, version 1.1.2). The preprocessed RNA-seq data were subjected to Generally Applicable Gene-set Enrichment (GAGE) with following the GAGE algorithms comparing the control and the treated group for each model (19). After adapting GAGE, we obtained lists of GO terms with the mean difference and associated p value for each model and time point. To summarize and prioritize GO terms, we computed rank product statistics utilizing the mean difference values extracted from samples obtained at 48 and 72 hours, aligning with the respective ALT peaks for each model (20).

Results

Establishment of a Drinking Water-Induced Liver Injury Model Using MDA

To develop a novel and practical model of liver injury that enables longitudinal investigation with minimal invasiveness, we screened candidate compounds from large-scale toxicology databases (14–16). Compounds were prioritized based on established hepatotoxicity profiles, availability of chronic administration data, and potential for solubility and stability in aqueous media. A literature survey, as detailed in the Methods section, guided the refinement process and led to the selection of 4,4'-methylenedianiline (MDA). MDA has been reported to exert pronounced hepatotoxicity and has previously been administered via drinking water in a carcinogenicity study in rats (13,21). Despite these findings, MDA has not been evaluated as a drinking water-based model compound for experimental hepatotoxicity.

To examine its potential for inducing liver injury in mice, we administered MDA through drinking water over a 28-Day period. In parallel, thioacetamide (TAA), a widely used hepatotoxicant, was administered using the same protocol to serve as a reference model. Serum biochemical analyses were conducted on Days 7, 14, and 28 to assess liver function. Both MDA- and TAA-treated groups showed significant elevations in alanine aminotransferase (ALT), a marker of hepatocellular injury (Fig. S2, Table 1, Table S2). Notably, the MDA-treated group consistently exhibited higher mean ALT levels than the TAA group across all time points, reaching statistical significance on Day 14.

To evaluate fibrotic responses, we performed qPCR for fibrosis-related genes. On Day 14, expression levels of Col1a1 and Acta2 were markedly increased in the MDA group compared to both the control and TAA groups (Fig. 1A, B), suggesting that MDA triggers peribiliary fibrotic remodeling. Taken together, these results indicate that MDA administration via drinking water can reliably induce liver injury with distinct pathological features. Hereafter, we designate these models as the MDA-DW and TAA-DW models, respectively.

Histopathological Analysis

To further characterize the pathological features induced by MDA administration, liver tissues were collected on Days 7, 14, and 28 and subjected to hematoxylin and eosin (H&E) and Sirius Red staining (Fig. 1C). Histopathological scores summarizing lesion severity and frequency are presented in Table S3 (a).

In the TAA-DW model, minimal to mild hepatocellular necrosis was predominantly observed in the centrilobular region, accompanied by mononuclear inflammatory cell infiltration and hepatocellular hypertrophy. These findings were present as early as Day 7 and remained largely unchanged in severity through Day 28. Oval cell hyperplasia, a regenerative response often associated with liver injury, was also evident in the centrilobular region, with a slight increase in both extent and frequency over time. These pathological features align with the known metabolic activation of TAA by CYP2E1, which is abundantly expressed in centrilobular hepatocytes and generates toxic intermediates that promote centrilobular injury (22). Additionally, focal hemorrhagic necrosis was noted on the visceral surface of the left lateral lobe at Day 7, which subsequently evolved into regions rich in hemosiderin-laden macrophages by Days 14 and 21.

In contrast, the MDA-DW model demonstrated a markedly different lesion distribution. Hepatic injury was localized primarily to the periportal region, where mild to moderate bile duct hyperplasia with degenerative changes was consistently observed across all examined time points. Surrounding these ducts, inflammatory cell infiltration and periportal fibrosis were frequently detected. These findings suggest that MDA causes direct epithelial damage to the bile ducts, provoking a reactive ductular response and fibrotic remodeling (23). In addition, MDA-treated animals exhibited mild to moderate focal hepatocellular necrosis on Days 7, 14, and 28. Unlike the stereotyped zonal injury patterns seen with many hepatotoxins, these necrotic lesions lacked clear spatial consistency and appeared irregularly scattered throughout the parenchyma. On Days 14 and 28, focal macrophage clusters were observed at sites of necrosis, suggesting engagement of phagocytic clearance mechanisms. Hepatocellular atrophy was also present throughout the administration period, potentially reflecting reduced glycogen content secondary to diminished food intake.

To evaluate fibrosis with greater specificity, Sirius Red staining was employed. In the TAA-DW model, only minimal pericellular fibrosis was observed in centrilobular zones in one animal at Days 14 and 21. In contrast, the MDA-DW model exhibited mild to moderate peribiliary fibrosis as early as Day 7, which persisted through Days 14 and 21. These observations were consistent with the fibrosis-related gene expression patterns described below and reinforce the distinction between the two models in terms of fibrosis distribution and severity. Detailed histopathological scoring is presented in Table S3(b-d).

Unsupervised Analysis of Toxicopathological Profiles

As described above, irregularly scattered necrotic lesions were observed in the MDA-DW model, differing notably from the necrotic patterns typically associated with drug-induced liver injury. To characterize these toxicopathological features from an alternative perspective, we performed an unsupervised analysis using a computer-vision approach. First, each WSI was subdivided into smaller units, known as patches. We then extracted latent representations from each patch, converting them into numeric vectors suitable for analysis. An anomaly detection algorithm was subsequently applied to these patch vectors, enabling visualization of abnormal regions within each WSI in an unsupervised manner.

The TAA-DW model displayed extensive anomalous regions concentrated in a single contiguous area,

whereas anomalous regions in the MDA-DW model were smaller and more diffusely scattered (Fig. 2A and B). Figure 2C and D show cropped images corresponding to the boxed regions in Fig. 2B. The cropped region from the TAA-DW model predominantly exhibited hemorrhagic necrosis, while irregularly scattered necrotic lesions were prominent in the MDA-DW model. Notably, the characteristic necrotic lesions in the MDA-DW model were relatively larger than typical cellular necrosis, as also evident at the WSI level (Fig. 2B). The total area of anomalous patches significantly increased in both treatment groups compared to controls, with a particularly pronounced elevation observed in the MDA group on Days 14 and 28 (Fig. 2E).

To investigate the heterogeneity of these lesions, we performed principal component analysis (PCA) on the patch vectors, revealing two distinct clusters corresponding to TAA-specific and MDA-specific lesions (Fig. 2F). Patch-level examination confirmed that TAA-specific clusters were characterized by extensive hemorrhagic necrosis, whereas MDA-specific clusters showed spatially dispersed focal hepatocellular necrosis of unclear etiology (Fig. 2G).

Together, this analysis provides quantitative support for the observation that the two models produce distinct pathological phenotypes.

Experimental Design for Comparing the Pathological Development Processes of MDA-DW and TAA-DW Models

Having established that the MDA-DW and TAA-DW models display clearly divergent pathological features over time, we sought to understand the mechanisms underlying these differences in the context of chronic disease progression. Our primary aim was to develop a model suitable for tracking liver injury longitudinally, and indeed, we observed spatially and temporally distinct patterns of necrosis, fibrosis, and biochemical alterations across the chronic phase. These findings prompted a deeper investigation into the earlier phases of liver injury, where molecular and cellular events may act as initiators that shape later outcomes.

To explore this hypothesis, we designed a comparative analysis focused on the early-phase dynamics of each model, aiming to uncover the micro-level processes that precede and potentially determine chronic pathological divergence. This analysis was structured around a multi-scale, multi-modal framework (Fig. 3), incorporating:

1. Plasma biochemical markers, which provide quantitative indicators of liver function and systemic responses to injury.
2. Immune cell profiling by flow cytometry, which reveals shifts in innate and adaptive immune populations in the liver.
3. Hepatic transcriptomic profiling, which reflects the molecular signatures associated with injury, inflammation, and tissue remodeling.

These three layers of data were acquired longitudinally from the same animals at five critical time points, enabling within-subject, time-resolved comparisons across biological scales. This integrative approach allowed us to track the emergence of model-specific pathophysiological trajectories from the earliest phases of injury, offering insights into how distinct molecular and immunological events may give rise to

the divergent chronic-phase phenotypes observed in the MDA-DW and TAA-DW models (Fig. 3).

Comparison of Plasma Biochemical Markers Between MDA-DW and TAA-DW Models

To assess systemic responses to liver injury, we first compared biochemical test results across the MDA-DW and TAA-DW models during the early administration phase. Both models showed elevated ALT levels indicative of hepatocellular damage, but the temporal dynamics and variability differed markedly (Table 2, Table S4). In the TAA-DW model, ALT levels peaked sharply on Day 2 with pronounced inter-individual variability, which then gradually declined over time. In contrast, the MDA-DW model displayed a more gradual increase, peaking on Day 3. Notably, the distribution of ALT values on Day 3 in the MDA group was bimodal, segregating animals into high and low ALT responders (Table 2, Table S4). This suggests underlying heterogeneity in susceptibility to MDA-induced injury or differences in exposure kinetics.

Despite continued compound administration, both models exhibited partial recovery of ALT levels by Day 8, indicating engagement of endogenous repair mechanisms. Importantly, the MDA-DW group also exhibited significant elevations in ALP, TBIL, and TCHO, markers of cholestatic liver dysfunction, which were less pronounced in the TAA-DW group (Table 2, Fig. S3). These findings are consistent with previous reports describing cholestatic features in MDA-induced toxicity following single-dose oral administration (10). Collectively, the MDA-DW and TAA-DW models demonstrate distinct biochemical profiles that reflect divergent pathophysiological processes.

Comparison of Immune Cell Profiles in MDA-DW and TAA-DW Models

Given the central role of immune responses in liver injury progression and resolution (24–28), we next investigated immune cell dynamics in the two models using flow cytometry. To explore global changes over time, we applied META visualization, an ensemble method integrating multiple dimensionality reduction techniques (17) for dimensionality reduction of cytometry data, enabling identification of broad immunological trends (Fig. 4A). Although treatment and control groups were indistinguishable in the early phase, temporal divergence emerged with continued exposure.

Zoomed-in analyses revealed shared and model-specific immune cell behaviors. Both models showed a consistent reduction in lymphocyte populations and an increase in neutrophils during peak ALT responses (Fig. 4B), with neutrophil proportions strongly correlating with ALT levels ($R = 0.82$). Kupffer cell populations decreased transiently on Days 2–3 and recovered by Day 4 (Fig. S4), suggesting temporary depletion or phenotypic shift due to acute inflammation.

In addition to shared responses, clear model-specific differences were identified. The TAA-DW group exhibited a transient elevation in eosinophils on Day 3, a phenomenon not observed in the MDA-DW model. Conversely, the MDA-DW group displayed a significant increase in CD8-positive T cells on Day 8, which was not evident in the TAA-DW model. These findings indicate that while both models activate common inflammatory cascades, they diverge in the recruitment and involvement of specific immune subsets, potentially reflecting differences in the spatial context and nature of the tissue injury.

Comparison of Hepatic Transcriptome Profiles in MDA-DW and TAA-DW Models

To examine molecular-level differences in the hepatic response to injury, we performed RNA sequencing on liver tissues from both models. Gene expression data were visualized using META visualization (Fig. 5A, B; see also Fig. S5). Samples collected shortly after compound administration clustered near control animals but diverged progressively over time. By Day 8, individuals with lower ALT levels tended to shift back toward the control cluster, whereas those with sustained liver injury remained distant. This pattern was observed regardless of the model, suggesting a tight coupling between functional injury and transcriptional disruption.

Interestingly, the transcriptomic divergence between models increased over time. On Day 3, distinct clusters were observed for MDA-DW and TAA-DW animals, underscoring differential gene regulatory programs in response to each compound. When visualized alongside ALT levels, animals with lower enzyme levels consistently resided closer to control-like transcriptomic states (Fig. 5B), confirming ALT as a surrogate marker of overall molecular trends.

To identify key biological processes underlying these transcriptomic shifts, we conducted Gene Set Analysis using the GAGE framework (19), which accommodates unbalanced sample sizes. In the MDA-DW model, IL-17-related and monocyte-associated Gene Ontology (GO) terms were significantly enriched during the acute phase (Days 2 and 3), consistent with our immune profiling results (Fig. 5C, Table S5). The TAA-DW model exhibited a similar enrichment trend, suggesting that some immune activation mechanisms are conserved across injury types (Table S6).

However, notable divergences emerged in the regulation of extracellular matrix-related pathways. Fibrinolysis-related GO terms showed opposite regulation directions between the two models—upregulated in MDA-DW and downregulated in TAA-DW (Fig. 5C). This suggests that matrix remodeling and resolution processes follow different trajectories depending on the nature and localization of liver injury. These molecular differences further reinforce the histological and immunological distinctions observed between the models.

Multi-Scale Characterization of Two Distinct Hepatotoxic Models

Together, these results reveal that the MDA-DW and TAA-DW models represent distinct pathological profiles, each characterized by unique patterns of biochemical, histological, and molecular responses to hepatotoxic compounds (Fig 6). While both models induce liver injury, their early-phase trajectories diverge across multiple biological layers: systemic liver function markers, immune cell dynamics, and hepatic transcriptome signatures. These early differences likely underpin the divergent histological outcomes observed during the chronic phase, including zonal distribution of necrosis, fibrosis localization, and cholestatic features. A multi-layered comparison of these models highlights their utility as complementary platforms for studying diverse aspects of liver pathophysiology, and suggests that the mechanisms set in motion during the early response phase may play a critical role in shaping long-term disease progression.

Discussion

In this study, we established a longitudinally tractable mouse model of liver injury through oral administration of 4,4'-methylenedianiline (MDA) via drinking water (MDA-DW model) and demonstrated its distinct pathophysiological characteristics compared to the widely used thioacetamide (TAA)-based model. This new model not only reflects characteristic features of hepatic injury such as hepatocellular necrosis and fibrosis, but also replicates elements of cholestatic liver injury, while providing significant advantages for longitudinal studies due to its low-cost and low-mortality nature.

A hallmark of the MDA-DW model is the emergence of temporally dynamic, spatially irregular focal hepatocellular necrosis, which was observed on Days 7, 14, and 28 (Fig. 1C, Fig. 2A, B, Table S3). Unlike classical chemical models where liver injury tends to localize within defined anatomical zones such as centrilobular or periportal areas, MDA-induced lesions were distributed irregularly and evolved over time. This suggests a mechanism of injury distinct from that observed in the TAA-DW model, which predominantly involves centrilobular necrosis. The focal nature of necrosis and the concurrent appearance of localized macrophage aggregations on Days 14 and 28 suggest ongoing tissue remodeling and immune-mediated clearance of damaged hepatocytes. The ability to induce such unique lesion patterns through a simple drinking water administration route highlights the practical and experimental value of the MDA-DW model.

Another important feature of the MDA-DW model is its cholestatic signature, evidenced by sustained elevations in ALP, TBIL, and TCHO, as well as the presence of peribiliary fibrosis seen histologically and supported by qPCR results for fibrosis markers. These features have not been previously replicated by drinking water-administered models and indicate a unique capability of the MDA-DW model to reproduce biliary-type injury. This has substantial implications for modeling cholestatic liver diseases such as primary biliary cholangitis (PBC) or primary sclerosing cholangitis (PSC), especially considering the challenges in creating longitudinal models of these conditions (29).

Model stability is essential for enabling reproducible and ethically manageable animal studies. The TAA-DW model, though widely adopted, is associated with high ALT elevations often exceeding 10,000 U/L and significant animal mortality (Table 2, Table S4) (30). In our experiments, the MDA-DW model induced liver injury with ALT levels averaging around 3,000 U/L, showing a more gradual elevation peaking on Day 3. Note that a bimodal distribution of ALT values was observed at this peak, reflecting inter-individual variability in susceptibility or exposure. The lower toxicity profile and absence of mortality make this model well-suited for long-term studies and for mechanistic investigations that require consistent and extended data acquisition.

This study also uncovered molecular insights into the pathogenesis of MDA-induced liver injury. Transcriptomic analysis revealed activation of IL-17 and monocyte-related gene signatures in the early stages (Days 2 and 3), implicating both adaptive and innate immune responses in the initial reaction to MDA exposure. Notably, gene sets associated with fibrinolysis were upregulated in the MDA-DW model but downregulated in TAA-DW, suggesting divergent pathways of extracellular matrix remodeling (Fig.

5C). Fibrin deposition is a recognized feature in several liver injury models and clinical cholangiopathies (31–34). Research by Luyendyk and others has linked fibrin accumulation to ductular reactions in ANIT-treated animals and patients with PBC and PSC (35–37). Considering that both ANIT and MDA disrupt bile ducts and cause focal necrosis, it is plausible that the MDA-DW model shares key histological features with ANIT-based models (37). ANIT has low solubility and the preparation of ANIT-containing diets is costly for longitudinal analysis. While we did not directly assess fibrin deposition histochemically, future validation of this aspect could further support the utility of the MDA-DW model in modeling fibrin-associated cholestatic liver pathology.

The regression of necrotic lesions over time, despite continuous exposure to MDA, offers a compelling view into tissue resolution dynamics under chronic injury conditions. In single-administration models, immune-mediated repair is often dominated by monocyte-derived macrophages and natural antibodies (NAbs), as shown in prior studies by Feng et al. (38) and Mattos et al (39). In our model, we observed progressive recruitment of monocyte-derived macrophages and changes in CD8+ T cell populations, implying active immunological participation in injury resolution (Fig. 4, Fig. S4). Strikingly, eosinophil infiltration was observed exclusively in the TAA-DW model but not in MDA-DW, further emphasizing distinct immune landscapes between the two models. Such immune cell differences could be linked to the different nature of liver injury—centrilobular and necrotic versus periportal and cholestatic—and may help clarify the immunopathology associated with various types of liver disease.

A unique strength of this study lies in its integrated, longitudinal design. Biochemical tests, immune cell profiles, and transcriptomic data were collected from the same animals at multiple time points, allowing for within-subject comparisons and high-resolution tracking of disease progression (Fig. 3). This approach not only reduces inter-animal variability but also enables detailed correlation between systemic markers (e.g., ALT), immune shifts, and transcriptional reprogramming. For instance, individuals with early ALT peaks were frequently associated with robust neutrophil responses and showed transcriptomic divergence from control-like profiles, highlighting the interdependence of systemic, cellular, and molecular-level responses. Such integrative data can serve as a basis for constructing predictive models of liver injury trajectories or evaluating therapeutic interventions across multiple biological scales.

In conclusion, the MDA-DW model introduced in this study represents a significant advancement in the field of experimental hepatology. By combining a simple and scalable administration method with the ability to replicate both necrotic and cholestatic liver injury features, this model provides a powerful platform for mechanistic and translational research. Its low toxicity and stability make it particularly suitable for longitudinal studies, and its unique immunopathological and transcriptomic features open new avenues for exploring liver disease pathogenesis. Future studies involving detailed histological evaluation of focal necrosis and fibrin deposition, as well as application to genetically modified mice or therapeutic interventions, will further extend the model's applicability—particularly in studying the temporal progression and resolution of liver disease in a longitudinal framework relevant to human pathophysiology.

Acknowledgements

We thank all those who contributed to the construction of the data sets employed in the present study such as CEBS, Open TG-GATEs, and DrugMatrix. We also thank Dr. Toru Komatsu (the University of Tokyo) for helpful discussion.

References

1. Balakrishnan M, Rehm J. A public health perspective on mitigating the global burden of chronic liver disease. Hepatology. 2024;79:451–459.

2. Ibrahim SH, Kamath BM, Loomes KM, Karpen SJ. Cholestatic liver diseases of genetic etiology: Advances and controversies. Hepatology. 2022;75:1627–1646.

3. Tsuchida T, Lee YA, Fujiwara N, Ybanez M, Allen B, Martins S, et al. A simple diet- and chemical-induced murine NASH model with rapid progression of steatohepatitis, fibrosis and liver cancer. J. Hepatol. 2018;69:385–395.

4. Scholten D, Trebicka J, Liedtke C, Weiskirchen R. The carbon tetrachloride model in mice. Lab. Anim. 2015;49:4–11.

5. Jaeschke H, Williams CD, Ramachandran A, Bajt ML. Acetaminophen hepatotoxicity and repair: the role of sterile inflammation and innate immunity. Liver Int. 2012;32:8–20.

6. Tanaka Y, Aleksunes LM, Cui YJ, Klaassen CD. ANIT-Induced Intrahepatic Cholestasis Alters Hepatobiliary Transporter Expression via Nrf2-Dependent and Independent Signaling. Toxicol. Sci. 2009;108:247–257.

7. Yang X, Greenhaw J, Shi Q, Roberts DW, Hinson JA, Muskhelishvili L, et al. Mouse Liver Protein Sulfhydryl Depletion after Acetaminophen Exposure. J. Pharmacol. Exp. Ther. 2013;344:286–294.

8. Heymann F, Hamesch K, Weiskirchen R, Tacke F. The concanavalin A model of acute hepatitis in mice. Lab. Anim. 2015;49:12–20.

9. Nakama T. Etoposide prevents apoptosis in mouse liver with ?-galactosamine/lipopolysaccharide-induced fulminant hepatic failure resulting in reduction of lethality. Hepatology. 2001;33:1441–1450.

10. Kwon S-B, Park J-S, Yi J-Y, Hwang J-W, Kim M, Lee M-O, et al. Time- and dose-based gene expression profiles produced by a bile-duct-damaging chemical, 4,4'-methylene dianiline, in mouse liver in an acute phase. Toxicol. Pathol. 2008;36:660–673.

11. Salguero Palacios R, Roderfeld M, Hemmann S, Rath T, Atanasova S, Tschuschner A, et al. Activation of hepatic stellate cells is associated with cytokine expression in thioacetamide-induced hepatic fibrosis in mice. Lab. Invest. 2008;88:1192–1203.

12. Wang X, Lopategi A, Ge X, Lu Y, Kitamura N, Urtasun R, et al. Osteopontin induces ductular reaction contributing to liver fibrosis. Gut. 2014;63:1805–1818.

13. Lamb JC, Huff JE, Haseman JK, Murthy AS, Lilja H. Carcinogenesis studies of 4,4'-methylenedianiline dihydrochloride given in drinking water to F344/N rats and B6C3F1 mice. Journal of toxicology and environmental health. 1986;18:325–337.

14. Waters M, Stasiewicz S, Merrick BA, Tomer K, Bushel P, Paules R, et al. CEBS--Chemical Effects in Biological Systems: a public data repository integrating study design and toxicity data with microarray and proteomics data. Nucleic Acids Res. 2008;36:D892-900.

15. Igarashi Y, Nakatsu N, Yamashita T, Ono A, Ohno Y, Urushidani T, et al. Open TG-GATEs: a large-scale toxicogenomics database. Nucleic Acids Res. 2015;43:D921-7.

16. Ganter B, Snyder RD, Halbert DN, Lee MD. Toxicogenomics in drug discovery and development: mechanistic analysis of compound/class-dependent effects using the DrugMatrix database. Pharmacogenomics. 2006;7:1025–1044.

17. Ma R, Sun ED, Zou J. A spectral method for assessing and combining multiple data visualizations. Nat. Commun. 2023;14:780.

18. Liberzon A, Subramanian A, Pinchback R, Thorvaldsdóttir H, Tamayo P, Mesirov JP. Molecular signatures database (MSigDB) 3.0. Bioinformatics. 2011;27:1739–1740.

19. Luo W, Friedman MS, Shedden K, Hankenson KD, Woolf PJ. GAGE: generally applicable gene set enrichment for pathway analysis. BMC Bioinformatics. 2009;10:161.

20. Eisinga R, Breitling R, Heskes T. The exact probability distribution of the rank product statistics for replicated experiments. FEBS Lett. 2013;587:677–682.

21. Kopelman H, Robertson MH, Sanders PG, Ash I. The Epping jaundice. British medical journal. 1966;1:514–516.

22. Ramaiah SK, Apte U, Mehendale HM. Cytochrome P4502E1 induction increases thioacetamide liver injury in diet-restricted rats. Drug Metab. Dispos. 2001;29:1088–1095.

23. Dugas TR, Santa Cruz V, Liu H, Kanz MF. Evaluation of the gender differences in 4,4'-methylenedianiline toxicity, distribution, and effects on biliary parameters. J. Toxicol. Environ. Health Part A. 2001;62:467–483.

24. Hossain M, Kubes P. Innate immune cells orchestrate the repair of sterile injury in the liver and beyond. Eur. J. Immunol. 2019;49:831–841.

25. Yang R, Tonnesseen TI. DAMPs and sterile inflammation in drug hepatotoxicity. Hepatol. Int. 2019;13:42–50.

26. Liu K, Wang F-S, Xu R. Neutrophils in liver diseases: pathogenesis and therapeutic targets. Cell. Mol. Immunol. 2021;18:38–44.

27. Saijou E, Enomoto Y, Matsuda M, Yuet‐Yin Kok C, Akira S, Tanaka M, et al. Neutrophils alleviate fibrosis in the CCl4‐induced mouse chronic liver injury model. Hepatol. Commun. 2018;2:703–717.

28. Hatada S, Ohta T, Shiratsuchi Y, Hatano M, Kobayashi Y. A novel accessory role of neutrophils in concanavalin A-induced hepatitis. Cell. Immunol. 2005;233:23–29.

29. Shetty S, Boyer JL. Bile acid metabolism and T cell responses in cholangiopathy: Not one-way traffic. J. Hepatol. 2019;71:657–659.

30. Nikolaev V, Kerimova M, Naydenova E, Ivanov E, Adjarov D. Biochemical changes in the rat after chronic thioacetamide intoxication. Toxicology. 1988;48:81–85.

31. Whipple GH, Hurwitz SH. FIBRINOGEN OF THE BLOOD AS INFLUENCED BY THE LIVER NECROSIS OF CHLOROFORM POISONING. J. Exp. Med. 1911;13:136–161.

32. Neubauer K, Knittel T, Armbrust T, Ramadori G. Accumulation and cellular localization of fibrinogen/fibrin during short-term and long-term rat liver injury. Gastroenterology. 1995;108:1124–1135.

33. Hewett JA, Roth RA. The coagulation system, but not circulating fibrinogen, contributes to liver injury in rats exposed to lipopolysaccharide from gram-negative bacteria. J. Pharmacol. Exp. Ther. 1995;272:53–62.

34. Okajima K, Harada N, Kushimoto S, Uchiba M. Role of microthrombus formation in the development of ischemia/reperfusion-induced liver injury in rats. Thromb. Haemost. 2002;88:473–480.

35. Kopec AK, Luyendyk JP. Role of Fibrin(ogen) in Progression of Liver Disease: Guilt by Association? Semin. Thromb. Hemost. 2016;42:397–407.

36. Luyendyk JP, Cantor GH, Kirchhofer D, Mackman N, Copple BL, Wang R. Tissue factor-dependent coagulation contributes to alpha-naphthylisothiocyanate-induced cholestatic liver injury in mice. Am. J. Physiol. Gastrointest. Liver Physiol. 2009;296:G840-9.

37. Luyendyk JP, Kassel KM, Allen K, Guo GL, Li G, Cantor GH, et al. Fibrinogen deficiency increases liver injury and early growth response-1 (Egr-1) expression in a model of chronic xenobiotic-induced cholestasis. Am. J. Pathol. 2011;178:1117–1125.

38. Feng D, Xiang X, Guan Y, Guillot A, Lu H, Chang C, et al. Monocyte-derived macrophages orchestrate multiple cell-type interactions to repair necrotic liver lesions in disease models. J. Clin. Invest. [Internet]. 2023;133. Available from: http://dx.doi.org/10.1172/JCI166954

39. Mattos MS, Vandendriessche S, Schuermans S, Feyaerts L, Hövelmeyer N, Waisman A, et al. Natural antibodies are required for clearance of necrotic cells and recovery from acute liver injury. JHEP Rep. 2024;6:101013.

Figures and Tables

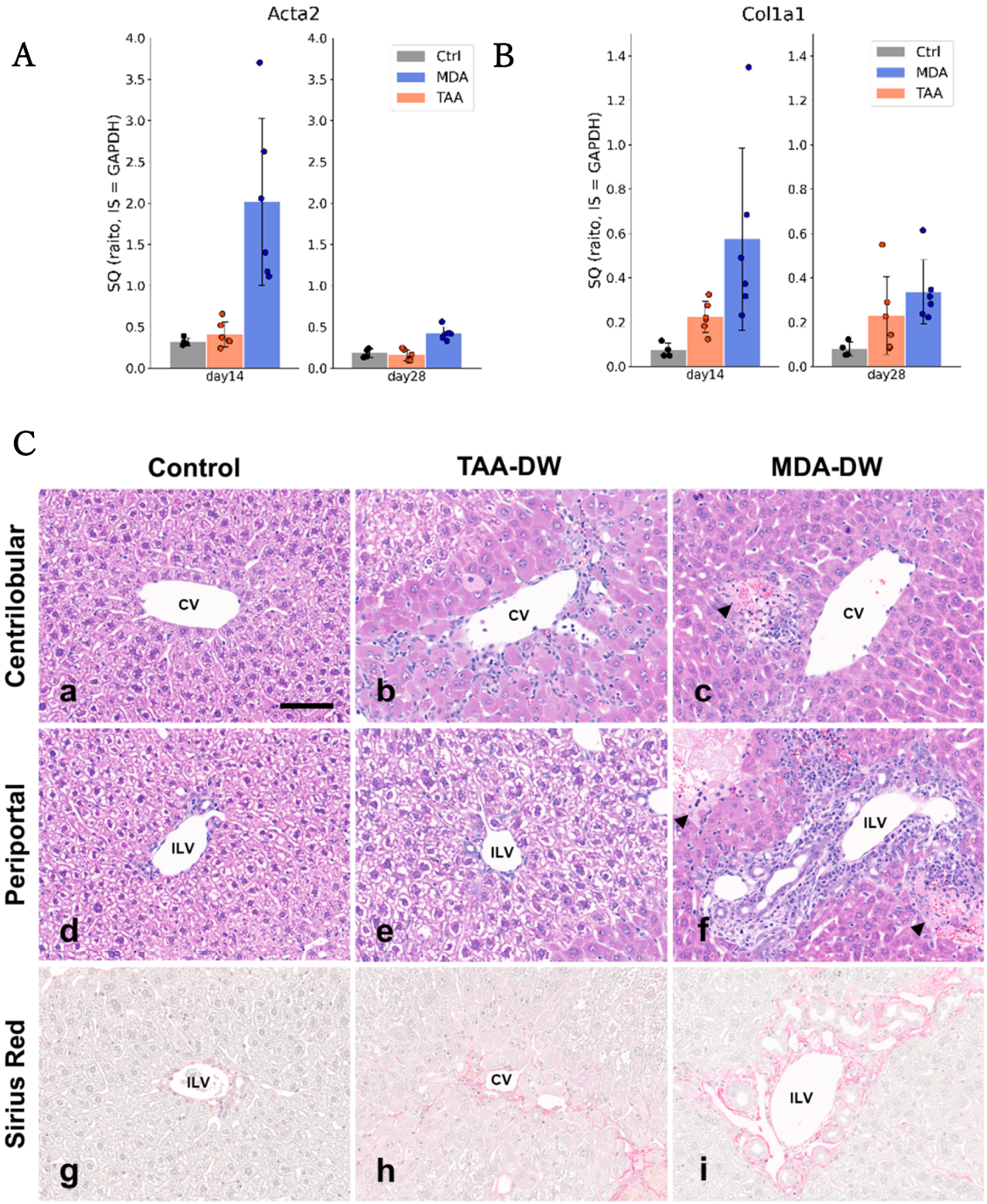

Fig. 1. Induction of liver injury via the oral administration of MDA in drinking water.
(A, B) Quantitative PCR evaluations of fibrosis markers at each time interval. Error bars represent standard deviation. (C) Images of H&E staining in the centrilobular (a-c) or periportal (d-f) regions on Day 7 and Sirius Red staining (g-i) on Day 28 are shown. Scale bar, 50 μm. Focal hepatocellular necrosis (arrowhead), CV: central vein, ILV: interlobular vein.

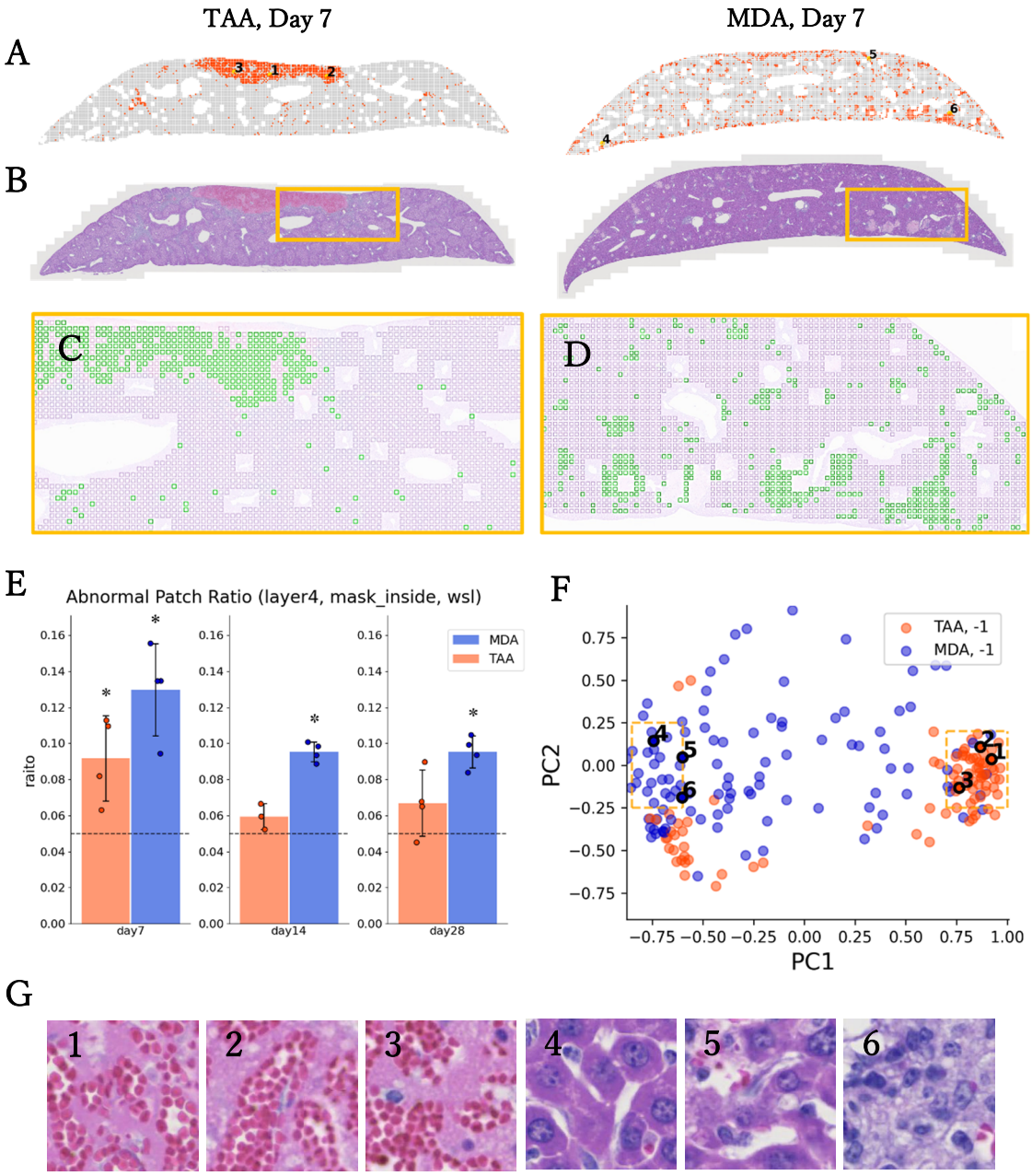

Fig. 2. Detection of abnormal regions in pathological images.
(A) Anomaly detection results on HE-stained images. Red highlights indicate regions identified as anomalous. (B) Original HE-stained image. (C, D) Overlays of the original image and anomaly detection results. Green frames mark patches classified as anomalous. (E) Proportion of patches classified as abnormal. The model was trained assuming 5% of patches in control images are abnormal. Statistical significance was assessed using a one-sample t-test. *$p < 0.05$. (F) PCA visualization of patch-level feature vectors and anomaly detection results (Day 7). A label of 1 denotes normal patches, and -1 denotes anomalous ones. (G) Cropped views of anomalous patches. Patch numbers correspond to those shown in panels (A) and (F).

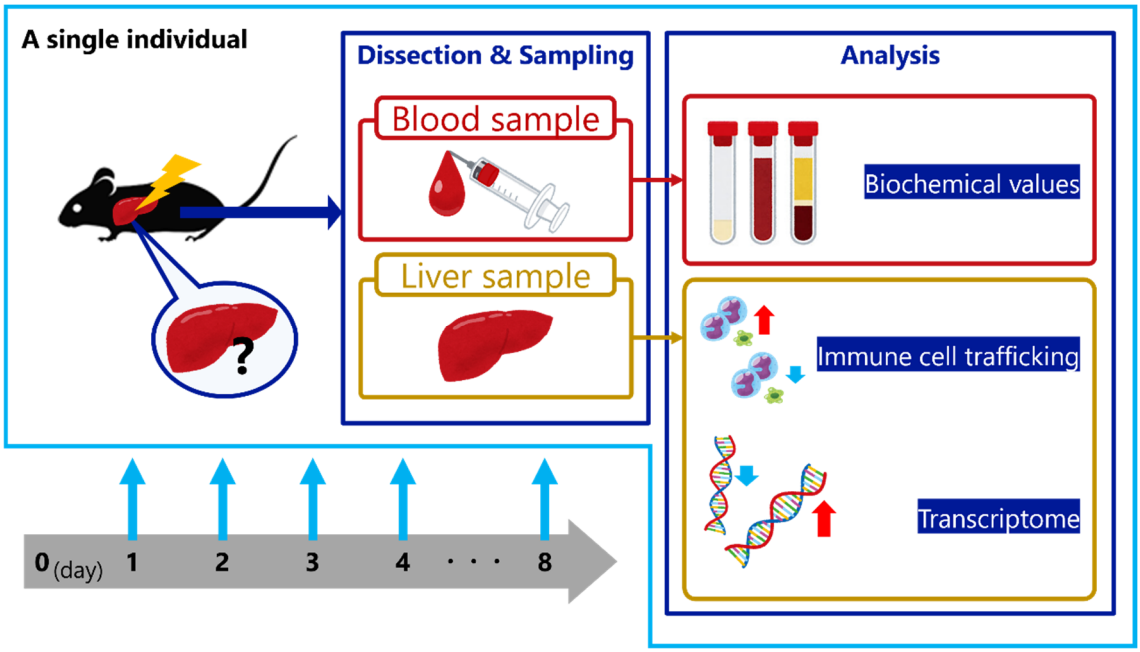

Fig. 3. Experimental design of multi-view data acquisition
Blood and liver samples are obtained from each individual to provide multi-view data linking the compound administered, time post-administration, blood biochemistry values, immune cell trafficking, and transcriptome data.

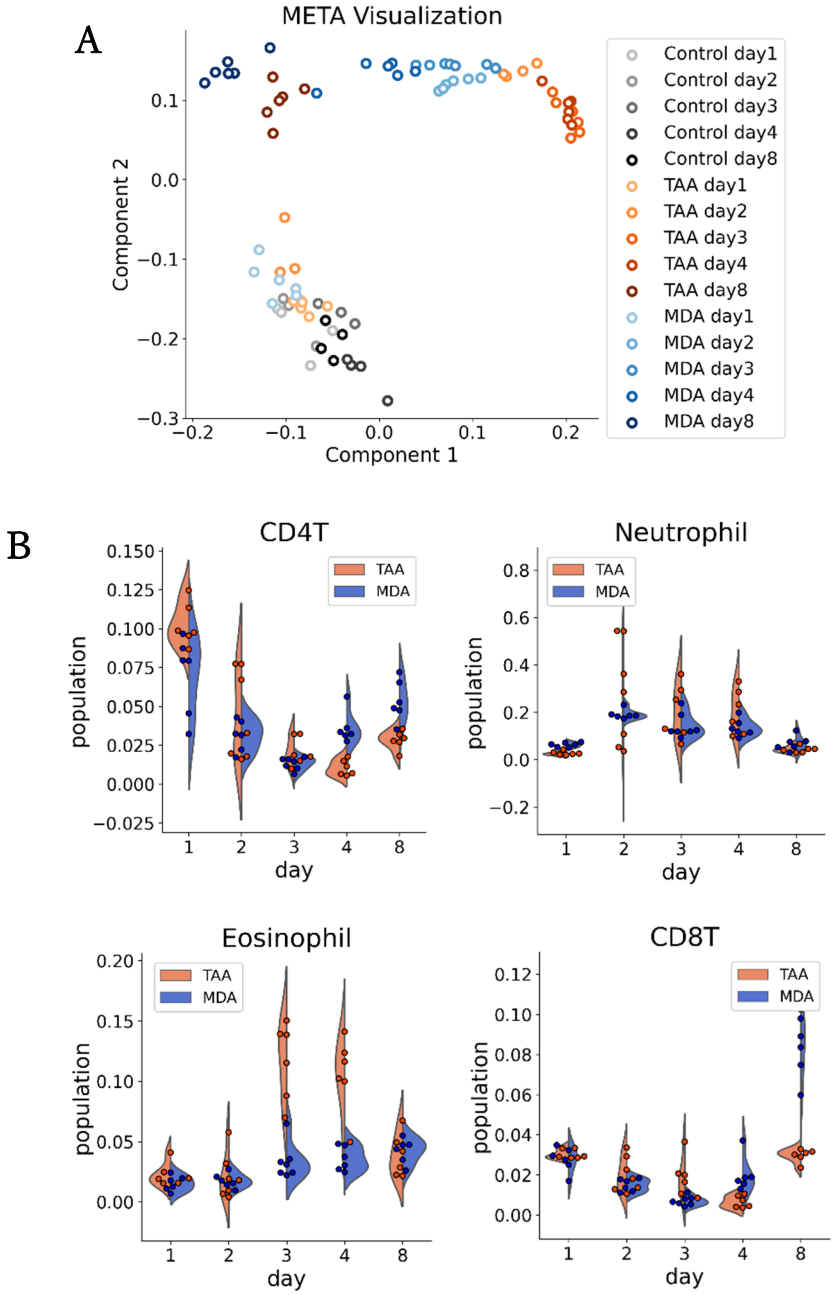

Fig. 4 Comparison of immune cell trafficking between MDA-DW and TAA-DW models
(A) immune cell trafficking data were embedded in two dimensions with meta-visualization, a dimensionality reduction method (1). (B) The violin plots represent the variation in immune cell proportion at different time points. It should be noted that the scale on the x-axis does not correspond to actual time.

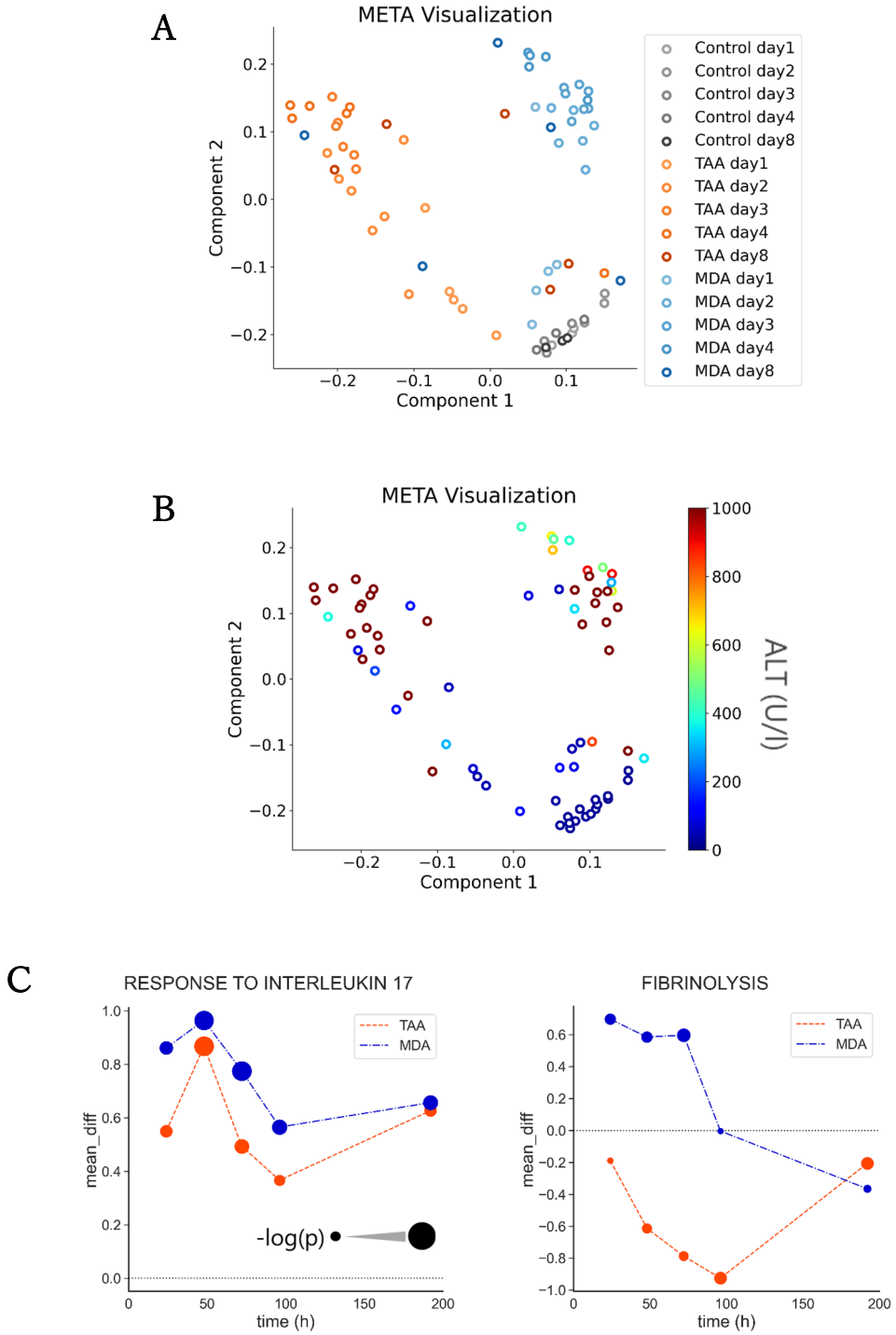

Fig. 5. Comparison of transcriptome profiles between MDA-DW and TAA-DW models
Transcriptome profiles were embedded into two dimensions with meta-visualization, a dimension-reduction method (1). The embedded values were plotted for visualizing two aspects: (a) temporal changes and (b) associations with ALT values. (c) Characteristic Gene Ontology (GO) terms associated with the MDA-DW and TAA-DW models are visualized. The vertical axis represents the GAGE mean difference, and the horizontal axis indicates time. The size of each circle corresponds to the –log(p) value calculated by GAGE.

	TAA-DW 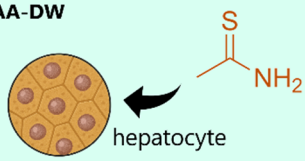	MDA-DW 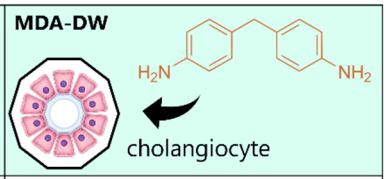
Cholestasis	absent	present
Fibrosis	minimal pericellular fibrosis	mild to moderate peribiliary fibrosis / Col1a1 and Acta2 were increased
Hepatocellular necrosis	centrilobular region	periportal region
Eosinophilic accumulation	notable on Day 3 and Day 4	-
CD8+ T cell accumulation	-	notable on Day 8
Response to IL17 (vs control)	⇧	⇧
Fibrinolysis (vs control)	⇩	⇧
mortality rate	low but not zero	no deaths have been observed to date

Fig. 6. Comparison of pathological profiles between MDA-DW and TAA-DW mode

Table 1: Blood biochemical values (chronic phase)

Data are presented as mean ± SD. Statistical significance was determined by one-way ANOVA followed by Tukey's HSD post hoc test. Adjusted p-values (*p-adj)* from the Tukey's HSD post hoc test score are indicated as follows: *, $p < 0.05$; **, $p < 0.01$; ***, $p < 0.001$.

Day	group	BW	ALT	p-adj	AST	p-adj
7	Control	20.5±0.2	26.0±1.8	-	43.8±3.9	-
	TAA	17.6±0.6	231.3±131.9	* vs Control	248.2±101.0	** vs Control
	MDA	19.0±1.1	326.3±65.5	*** vs Control	252.7±52.5	** vs Control
14	Control	21.7±0.3	28.3±4.0	-	40.8±7.1	-
	TAA	19.1±0.5	84.7±20.3	** vs Control	88.3±19.7	-
	MDA	21.5±0.9	223.5±29.2	*** vs Control, TAA	148.7±75.3	* vs Control
28	Control	23.7±0.2	24.3±0.5	-	32.5±1.3	-
	TAA	20.7±0.8	76.3±18.6	-	61.7±12.5	-
	MDA	21.1±0.5	135.3±75.8	** vs Control	144.8±60.9	** vs Control, TAA

Supplementary Information for "Establishment of a longitudinally tractable mouse model of cholestatic liver injury via drinking water administration of MDA"

Takumi Iwasaka[1], Katsuhisa Morita[1], Iori Azuma[1], Tomoka Nakagawa[1], Eri Nakashima[1], Tomomi Kamei[2], Yuki Kato[2], Hiroyuki Kusuhara[1], Tadahaya Mizuno[3, †]

[1]Graduate School of Pharmaceutical Sciences, the University of Tokyo, Bunkyo-ku, Tokyo, 113-0033, Japan
[2]Laboratory for Drug Discovery and Development, SHIONOGI & Co.,Ltd. Toyonaka, Osaka, 561-0825, Japan,
[3]Graduate School of Pharmaceutical Sciences, the University of Tokyo, Bunkyo-ku, Tokyo, 113-0033, Japan, Electronic address: tadahaya@gmail.com
†Corresponding author: Tadahaya Mizuno

Supplementary Methods

RNA-seq analysis

Poly(A) tailed mRNA was purified from total RNA prepared with Isogen II (311-07361, Nippon Gene, Japan) using the NEBNext Poly(A) mRNA Magnetic Isolation Module. RNA-Seq libraries were prepared using the NEBNext Ultra II Directional RNA Library Prep Kit for Illumina. Libraries were sequenced using the NovaSeq 6000 S1 Rgt Kit v1.5 (200 cyc).

Quality control of all reads was performed using PRINSEQ++ (version 1.2.4) with the indicated parameters (trim_left=5, trim_tail_right=5, trim_qual_right=30, ns_max_n=20, min_len=30) (https://peerj.com/preprints/27553/). The Expression of transcripts was quantified using Salmon (version 1.6.0) and gencode.vM28.transcripts obtained from GENCODE (https://www.gencodegenes.org/) with the indicated parameters (validationMappings, gcBias, seqBias) and decoy-aware index created using Salmon and GRCm39.primary_assembly.genome obtained from GENCODE (1). Transcripts Per Kilobase Million (TPM) data was obtained using tximport which is implemented in the software package Bioconductor with R (version 4.2.3) from quant.sh files created by Salmon (version 1.8.0)(2).

Histopathology

The left lateral lobe of the liver was excised and collected for histological analysis into a 5 mL tube containing 4 mL of 10% neutral-buffered formalin. Samples were fixed for 24 hours, washed with PBS for 2 hours, and subsequently stored in 70% ethanol. Tissue processing, sectioning, and staining with hematoxylin and eosin (H&E) or Sirius Red were outsourced to Genostaff Inc.

Tissue sections were prepared by longitudinally slicing the left lateral lobe. Fixed liver tissues were subjected to a standard dehydration and paraffin embedding protocol. Samples were first immersed in 70% ethanol at 4 °C for 3 days, followed by sequential incubations in 80%, 90%, and 100% ethanol for 1 hour each at room temperature (RT).

Subsequent processing was performed using an automated tissue processor (CT-Pro20, Genostaff Inc.). Tissues underwent three consecutive immersions in 100% ethanol (1.5 hours each at RT), followed by incubation in a 1:1 mixture of 100% ethanol and G-Nox (xylene substitute, Genostaff Inc.) for 1.5 hours at RT. Samples were then immersed sequentially in three changes of G-Nox (1.5 hours each at RT), and finally in three changes of paraffin wax at 65 °C for 1.5 hours each.

Paraffin blocks were sectioned at a thickness of 4 μm and used for both H&E and Sirius Red staining. For H&E staining, tissue sections were deparaffinized with xylene, rehydrated through a graded ethanol series, and rinsed in running tap water for 5 minutes, followed by distilled water. Sections were stained with hematoxylin (Sigma) for 3 minutes, rinsed in running tap water for 20 minutes, stained with eosin alcohol (Sigma) for 3 minutes, and then mounted with Malinol (#2040, Muto).

For Sirius Red staining, deparaffinized tissue sections were stained in Iron Hematoxylin Working Solution (Weigert's Iron Hematoxylin #4034, Muto Pure Chemicals) for 3 minutes at RT, treated with hydrochloric acid ethanol solution for 3 minutes, and rinsed in running tap water followed by distilled water. After treatment with 5% phosphomolybdic acid solution (#27615, Nacalai Tesque) for 2 minutes at RT, the sections were stained in saturated picric acid containing 0.1% Sirius Red (#3306, Muto) for 90 minutes at RT. They were then rinsed in 0.5% hydrochloric acid solution for 1 minute, dehydrated in three changes of 100% ethanol and xylene, and finally coverslipped with Malinol (#2040, Muto).

Stained sections were examined microscopically in a non-blind manner by two pathologists. One was a veterinary pathologist with 3 years of experience, and the other was a certificated veterinary/toxicology pathologist with over 15 years of experience. The histopathological scores were established as follows: 0 - no change; 1 - minimal change; 2 - mild; 3 - moderate change; 4 - marked change; 5 - severe change. Sirius Red was also used to semi-quantify the extent of fibrosis.

Flow cytometry analysis

The liver sample was dissociated using gentleMACS according to the manufacturer's instructions. Except noted especially, PBS containing 2% fetal bovine serum was used as "Wash Buffer" thereafter. The washed samples were centrifuged (50×g, 4 °C for 3 min) to eliminate hepatocytes and were subjected to ACK Lysis Buffer. ACK buffer was prepared by adding 8,024 mg of NH4Cl (A2037, TCI, Japan), 10 mg of NHCO3 (166-03275, FUJIFILM Wako, Japan), and 3.772 mg of EDTA 2Na · 2H2O (6381-92-6, Dojindo Laboratories, Japan) into 1 L pure water. The samples were washed with the Wash Buffer three times and then the samples were subjected to flow cytometry analysis. Flow cytometric analysis was performed with FACSCelesta (BD Biosciences, USA), and data were analyzed with FlowJo software (Treestar). Proportions of NK cells (CD45+/CD3−/NK1.1+), B cells (CD45+/B220+), CD4+ T cells (CD45+/CD3+/B220−/CD4+), CD8+ T cells (CD45+/CD3+/B220−/CD4−/CD8a+), NKT cells

(CD45+/CD3+/B220−/CD4−/CD8a−/NK1.1+), γδT cells (CD45+/CD3+/B220−/CD4−/CD8a−/gdTCR+), eosinophils (CD45+/CD11b+/Siglec-F+), neutrophils (CD45+/CD11b+/Siglec-F−/Ly6G+/Tim4−), monocytes (CD45+/CD11b+/Siglec-F−/Ly6G−/Tim4−/Ly6C+), monocyte-derived macrophages (CD45+/CD11b+/Siglec-F−/Ly6G−/Tim4−/Ly6C−), and Kupffer cells (CD45+/CD11b+/Siglec-F−/Ly6G−/Tim4+/Ly6C−) were acquired via flow cytometry. The antibodies used are listed in Supplementary Table S7.

Histopathological analysis with a deep learning model

The deep learning framework PyTorch version 2.0.1 was employed for this study. Deep learning and feature extraction tasks were carried out utilizing the FUJITSU Supercomputer PRIMEHPC FX1000 and FUJITSU Server PRIMERGY GX2570 (Wisteria/BDEC-01) at the Information Technology Center, The University of Tokyo. Python (version 3.11.3) with open-source packages was utilized for all analyses except for deep learning.

Pathological images of the liver were collected from the Open TG-GATEs (TGGATEs) database, along with corresponding pathological finding type annotations and individual rat information from TogoDB. These images were acquired at 20× magnification using Aperio ScanScope AT. The dataset preparation involved excluding compounds not sampled at all specified time points and limiting samples to the highest compound concentration. Subsequently, one control sample per condition and one image per individual were randomly selected, resulting in a dataset of 6508 whole slide images (WSI) for the liver. The construction of the finding-based model followed our previous work on expression learning based on pathological findings (3), with some differences such as varying image sizes and multi-label learning. The Open TG-GATEs dataset was split into Train1 and Test subsets in a 4:1 ratio, further split into Train2 and Validation subsets in a 4:1 ratio. Weak labels were generated through multi-label training using patches of pathological images and corresponding labels from the Train2 subset, focusing on eight pathological findings: proliferation bile duct, ground glass appearance, increased mitosis, inclusion body intracytoplasmic, deposit pigment, single cell necrosis, vacuolization cytoplasmic, and swelling. The model predicted the probability of these findings in images of the validation subset, repeated five times to apply resulting labels to Train1 subset patches. Patches were extracted based on predicted probabilities, and a new model was trained using these patches and corresponding probabilities for training of the

finding-based model.

The formalin-fixed liver specimens underwent standard processing procedures, including slicing into 4 μm sections, staining with hematoxylin and eosin (H&E), and visualization using ZEISS Axio Scan.Z1. Subsequently, the whole slide images (WSI) were partitioned into patches of 256×256 pixels, and feature extraction was performed on each patch using the aforementioned model. After extracting features from the fourth layer, one class support vector machine (sklearn, version 1.4.1) was employed to classify whether each patch was anomalous or not. Additionally, dimensionality reduction of the features was achieved through PCA and visualized. Details are available on our GitHub repository (https://github.com/mizuno-group/MDAdrinkingwater).

Supplementary Figures and Tables

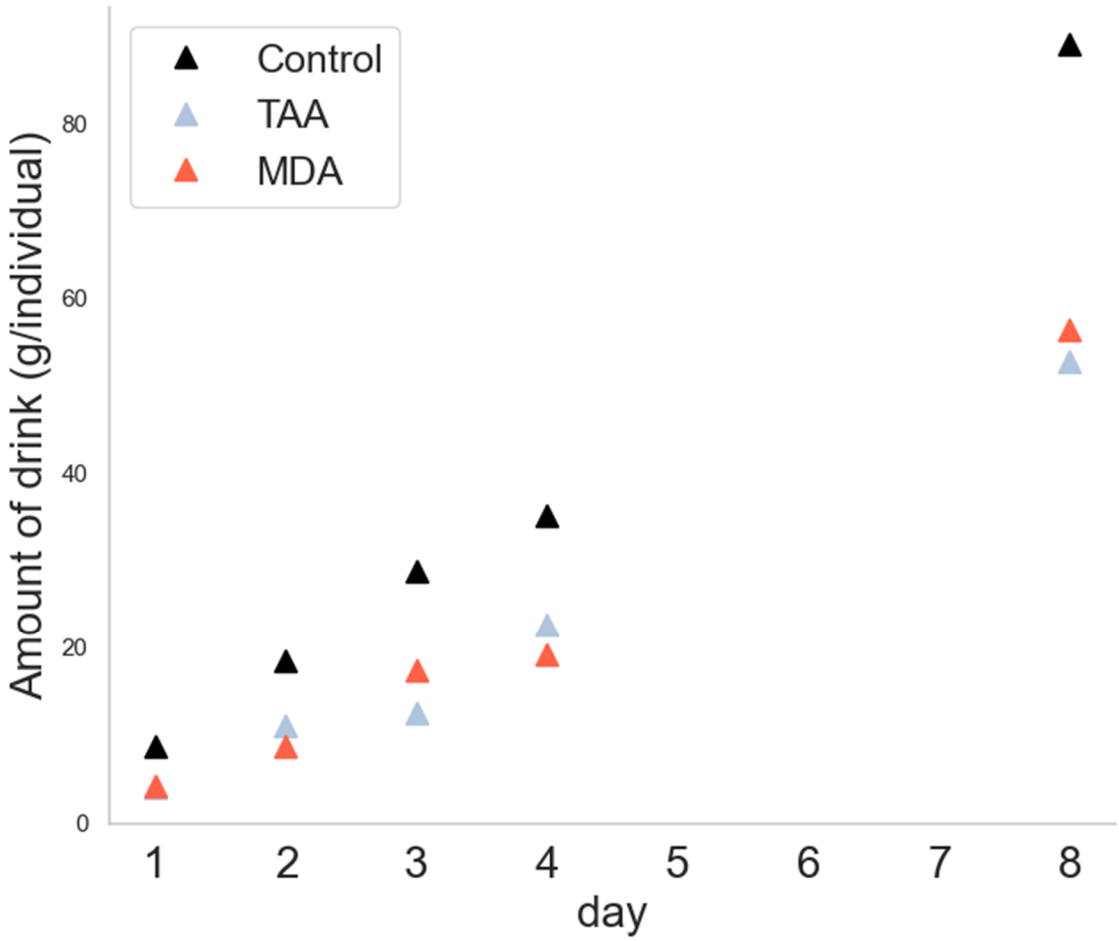

Fig. S1. Temporal changes in drinking water volume.
Plotting the amount of water consumed per cage normalized by the number of individuals.

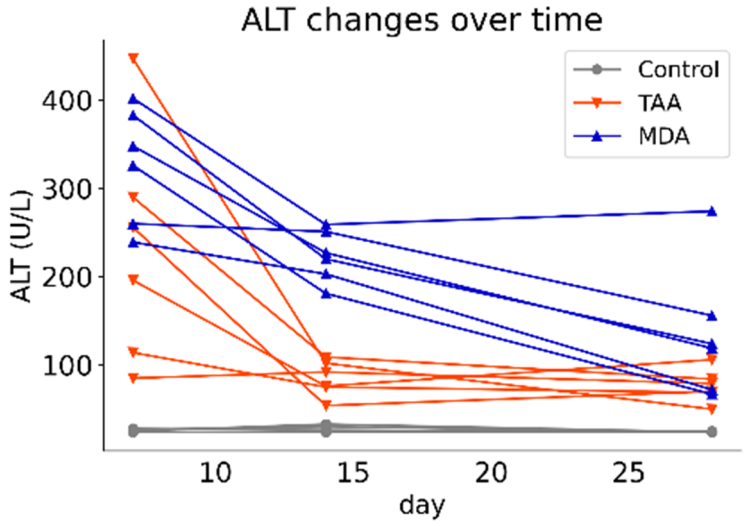

Fig. S2. Induction of liver injury via the oral administration of MDA in drinking water.
Time course of changes in alanine aminotransferase (ALT).

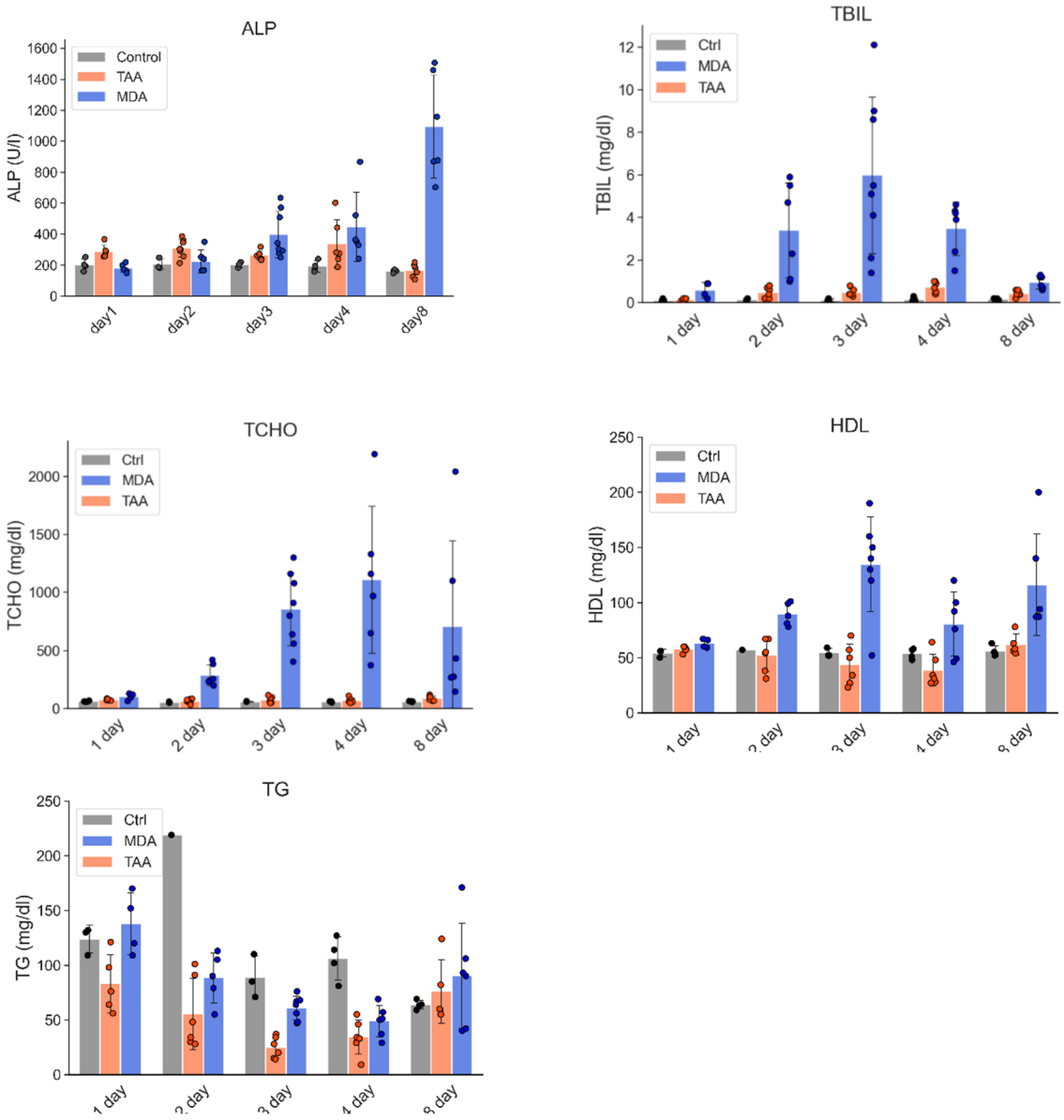

Fig. S3. Comparison of changes in blood biochemistry values between MDA-DW and TAA-DW models.

The figure illustrates the time course of changes in blood biochemistry values. Error bars are indicative of standard deviation. It should be noted that the scale on the x-axis does not correspond to actual time.

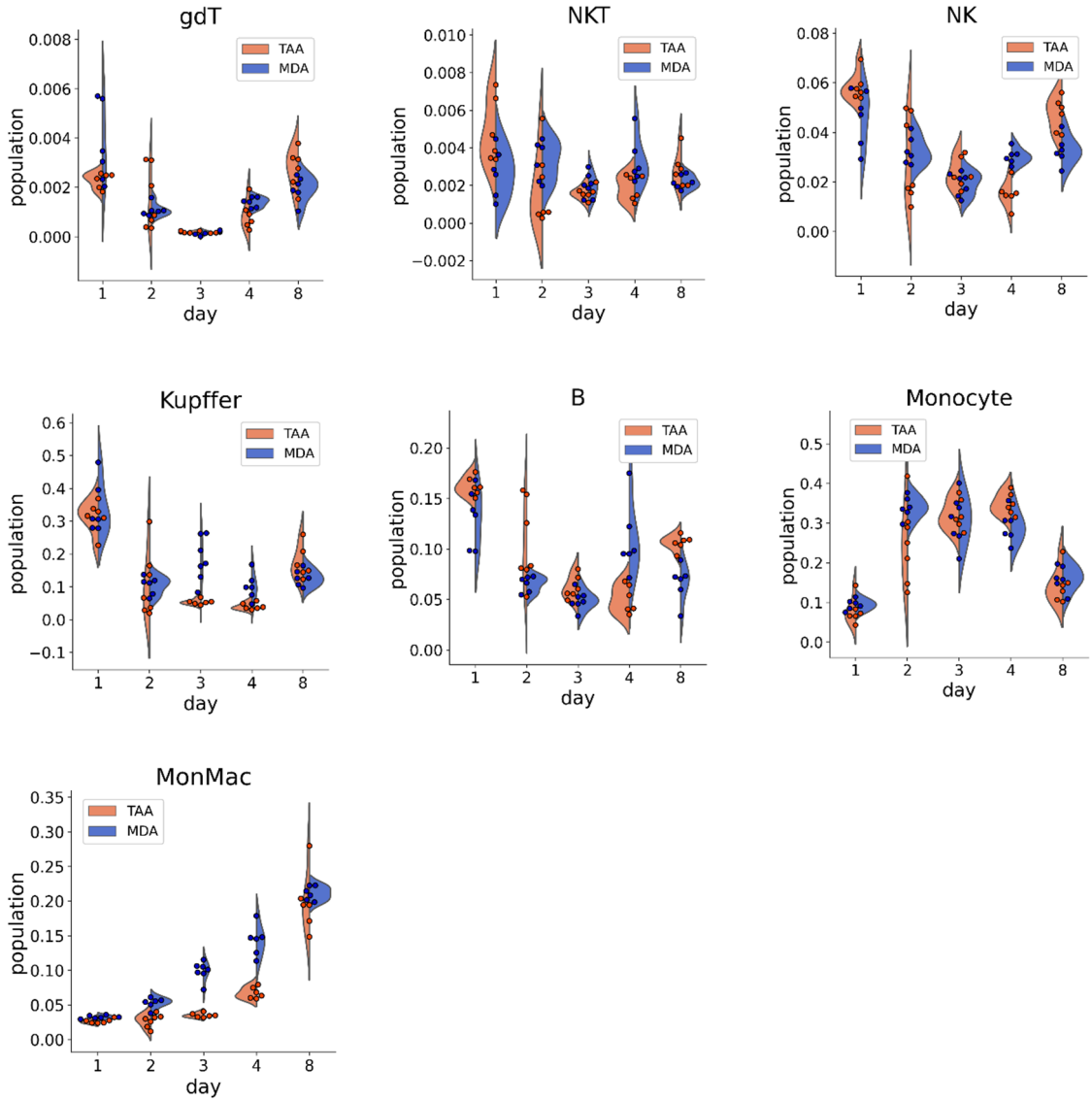

Fig. S4. Violin plot for immune cell populations after administration.
The violin plots represent the variation in immune cell proportion at different time points. It should be noted that the scale on the x-axis does not correspond to actual time. MonMac, monocyte-derived macrophages.

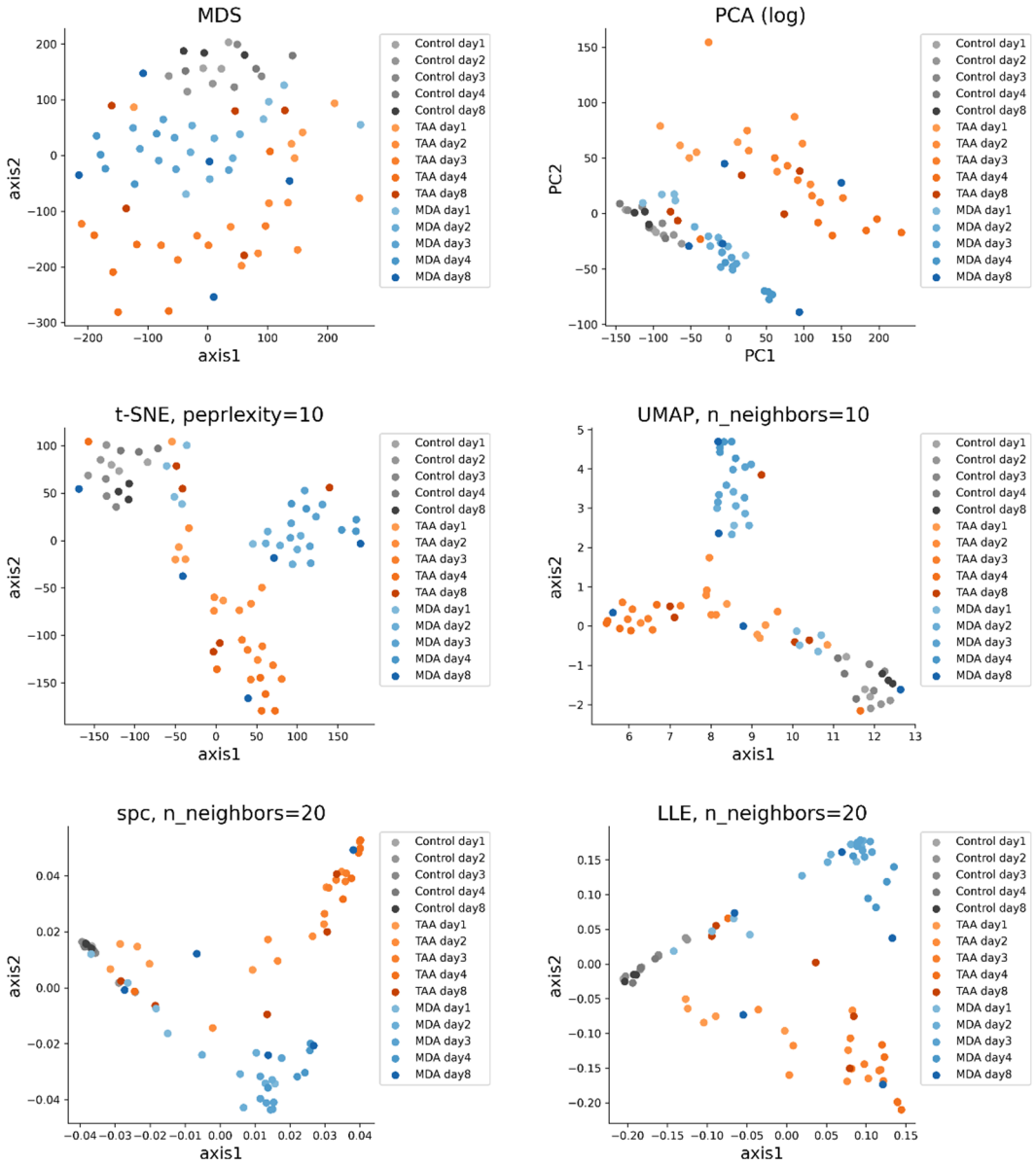

Fig. S5. Visualization of transcriptome data embedded in 2D with each method constituting meta-visualization.

The numerical value provided alongside the title represents the specified hyperparameter value. PCA, principal component analysis; MDS, multidimensional scaling; t-SNE, t distributed stochastic neighbor embedding; UMAP, uniform manifold approximation and projection; spc, spectral embedding; LLE, locally linear embedding.

References

1. Frankish A, Diekhans M, Ferreira A-M, Johnson R, Jungreis I, Loveland J, et al. GENCODE reference annotation for the human and mouse genomes. Nucleic Acids Res. 2019;47:D766–D773.
2. Patro R, Duggal G, Love MI, Irizarry RA, Kingsford C. Salmon provides fast and bias-aware quantification of transcript expression. Nat Methods. 2017;14:417–419.
3. Maedera S, Mizuno T, Kusuhara H. Investigation of latent representation of toxicopathological images extracted by CNN model for understanding compound properties in vivo. Comput Biol Med. 2024;168:107748.

Table 2: Blood biochemical values (acute phase)
Values are presented as mean ± SD. For parameters with only one or two samples (n = 1 or 2), values represent the mean without SD. Bold values indicate peak measurements observed during the treatment period under each condition.

group	Day	BW	ALT	AST	ALP	TBIL	TCHO	HDL	TG
Control	1	22.0±0.7	23.3±4.0	33.8±3.9	202.5±38.4	0.13±0.05	**63.5±4.7**	54.0±3.5	123.7±
	2	21.1±0.4	23.0±1.7	32.7±0.6	**206.3±37.1**	0.15	56.5	57.0	219.
	3	20.7±0.1	**26.0±2.6**	37.0±3.0	203.0±18.1	0.13±0.06	62.7±2.9	54.3±4.0	88.7±1
	4	20.6±0.5	23.8±1.0	33.8±1.5	192.5±35.7	0.15±0.10	59.3±5.2	53.5±4.8	106.0±
	8	20.5±0.6	25.3±1.0	**38.0±1.4**	161.5±9.7	**0.18±0.05**	62.5±3.4	55.8±5.0	63.8±
MDA	1	20.2±0.7	82.2±36.7	163.2±88.8	181.0±27.9	0.60±0.36	103.5±29.0	63.0±4.1	**137.8±**
	2	18.3±1.0	**1403.3±336.8**	**1861.7±443.5**	223.8±73.8	3.42±2.22	289.3±90.3	89.4±10.4	88.4±2
	3	17.3±0.7	1388.8±1174.4	1205.0±1107.1	398.1±149.8	**5.99±3.66**	856.9±312.5	**134.6±42.9**	60.9±1
	4	16.9±0.9	604.0±290.6	767.8±419.3	446.8±224.9	3.48±1.24	**1112.3±630.9**	80.5±29.2	48.8±1
	8	19.9±2.4	393.3±92.6	261.3±62.2	**1095.0±333.9**	0.97±0.30	710.5±734.7	116.0±46.0	90.3±4
TAA	1	20.9±0.7	62.2±27.9	70.8±24.7	287.5±42.5	0.15±0.05	76.8±7.3	57.6±2.9	**83.0±2**
	2	18.8±1.7	**21197.5±20513.4**	**16836.0±16630.7**	308.4±56.3	0.49±0.27	63.5±18.8	52.0±14.8	55.3±3
	3	18.8±0.9	4463.3±1120.9	2523.3±1343.4	264.8±30.3	0.48±0.18	78.0±27.2	43.5±18.5	24.7±
	4	17.0±0.4	2862.7±1419.2	2733.0±1632.3	**338.8±155.1**	**0.75±0.26**	71.0±22.0	38.7±14.6	34.3±1
	8	18.2±1.9	231.0±299.2	299.8±222.8	164.5±43.3	0.43±0.15	**90.3±21.8**	**61.8±9.7**	76.0±2